Appl. Math. Mech. -Engl. Ed., **45**(9), 1595–1612 (2024)

APPLIED MATHEMATICS AND MECHANICS (ENGLISH EDITION)

https://doi.org/10.1007/s10483-024-3139-6

Optimization for sound insulation of a sandwich plate with a corrugation and auxetic honeycomb hybrid core*

Fenglian LI†, Yiping WANG, Yuxing ZOU

School of Mechanical and Electrical Engineering, Beijing Information Science and Technology University, Beijing 100192, China

(Received Mar. 28, 2024 / Revised May 28, 2024)

Abstract A sandwich plate with a corrugation and auxetic honeycomb hybrid core is constructed, and its sound insulation and optimization are investigated. First, the motion governing equation of the sandwich plate is established by the third-order shear deformation theory (TSDT), and then combined with the fluid-structure coupling conditions, and the sound insulation is solved. The theoretical results are validated by COMSOL simulation results, and the effects of the structural parameter on the sound insulation are analyzed. Finally, the standard genetic algorithm is adopted to optimize the sound insulation of the sandwich plate.

Key words optimization, sound insulation, hybrid core layer, genetic algorithm

Chinese Library Classification O328
2010 Mathematics Subject Classification 74H45

1 Introduction

With the development of material science, sandwich panel structures have gained recognition for their unique core properties, lightweight, high specific rigidity and strength, vibration and noise reduction, and high load-carrying efficiency, and have been utilized in a variety of applications such as aerospace vehicles, high-speed trains, and military marine equipment[1–2]. However, traditional simple sandwich panels have drawbacks as they are difficult in meeting the usage requirements of complex working conditions. For example, corrugated sandwich panels have high stiffness but poor energy absorption capabilities. In recent years, there has been research on the development of novel mixed core layers by combining geometrically simple core layers into complex structures, inheriting properties from different component parts and even demonstrating superior performances beyond the original structure. Sandwich panels composed of mixed core layers have great potential for development and application and have gradually become a research hotspot both domestically and internationally.

* Citation: LI, F. L., WANG, Y. P., and ZOU, Y. X. Optimization for sound insulation of a sandwich plate with a corrugation and auxetic honeycomb hybrid core. *Applied Mathematics and Mechanics* (*English Edition*), **45**(9), 1595–1612 (2024) https://doi.org/10.1007/s10483-024-3139-6

† Corresponding author, E-mail: lifenglian@126.com

Project supported by the National Natural Science Foundation of China (Nos. 12172339 and 11732005) and the Beijing Natural Science Foundation of China (No. 1222006)

The performance of the core layer plays a decisive role in the sandwich structure. In practical models, the core layer can be equivalent to the homogeneity by the equivalent method. Hohe and Becker[3] adopted a homogenization scheme to obtain the equivalent elastic modulus, Poisson's ratio, and other parameters of a two-dimensional (2D) honeycomb structure. Zhuang et al.[4] homogenized the trapezoidal corrugated core into equivalent orthogonal layers based on the energy method, derived the equivalent elastic parameters, and improved the design calculation efficiency of trapezoidal corrugated sandwich plates. With more and more related studies, sandwich structures with complex cores of various shapes and structures have been designed and manufactured. Hou et al.[5] studied the mechanical properties of the hyperbolic honeycomb sandwich structure, established an equivalent mechanical model, and carried out an optimal design for weight. Shen et al.[6] set up a theoretical model of sound transmission loss (STL) for sandwich plates with lightweight two-leaf structures, and studied the acoustic and vibration characteristics of the structures. Han et al.[7–8] proposed the concept of combining metal honeycomb with corrugation sheet to build a corrugation-honeycomb hybrid structural core, and the results showed that compared with empty corrugated or honeycomb cores, the composite core layer had a larger compressive strength and a better energy absorption capacity. Zhang et al.[9] adopted the homogenization method to derive the equivalent elastic constant of the corrugation-honeycomb mixed core, and studied the vibration characteristics of the laminated beam with a mixed core. Zhang et al.[10] analyzed the structural strength and absorptivity of a high-density sandwich plate with a square honeycomb-corrugation mixed core, and showed that the core layer had greater effects on the structural performances.

In recent years, a novel material, which has a negative Poisson's ratio (NPR) or auxetic property, has attracted wide attention due to its strong shear modulus, impact strength, and indentation resistance. Liu and Liu[11] applied the bionics principle to propose an improved diabole-shaped NPR honeycomb structure, and studied its energy absorptivity and stability. Li et al.[12] studied the effects of an NPR material on the thermo-mechanical properties of cracked brittle honeycomb. Shao et al.[13] analyzed the compression performance of a gradient arranged NPR honeycomb plate. Xiao et al.[14] investigated the buckling characteristics of the NPR honeycomb structure. Xu et al.[15] studied the impact response of an NPR honeycomb structure with sinusoidal shape, and carried out optimization research. Li et al.[16] analyzed the vibro-acoustic performances of the NPR honeycomb sandwich plates with different configurations.

Sandwich plate structures have been widely used in many engineering fields. However, under real complex conditions, noise and vibration will have a great effect on the structures. Hence, it is of great significance to study the vibro-acoustic characteristics of these structures. Xin and Lu[17] investigated the sound radiation of sandwich structures under the excitation of simple harmonic point forces. Lin et al.[18] studied the sound insulation performance of a three-period minimal surface sandwich plate. Griese et al.[19] used a structural-acoustic finite element analysis (FEA) to systematically study the effects of honeycomb cores on the STL and vibration characteristics of sandwich plates. Meng et al.[20] studied the sound performances of perforated sandwich plates with various honeycomb shapes. Oliazadeh et al.[21] calculated the STL of honeycomb sandwich plates filled by foams, and carried out experimental verification. Xue et al.[22–23] analyzed the acoustic properties of the tunable magnetorheological metamaterial plate. Dong et al.[24] developed a general methodology for generating ultra-broadband achromatic metasurfaces with prescribed ultra-broadband achromatic properties in a bottom-up inverse-design paradigm. Yuan et al.[25] investigated the vibration and acoustic properties of porous foam functionally graded plates under the temperature field, and discussed the effects of the parameter on the sound insulation. Fu et al.[26] analyzed the sound radiation behavior of the sandwich structure with a truss core under thermal environment and the effects of the key parameters. Song et al.[27] studied the vibro-acoustic responses of a metamaterial sandwich plate with periodically connected resonant units.

With the wide applications of sandwich structures in engineering, how to improve the sound

insulation performance of a structure and how to reduce its density and cost have attracted more and more attention. Thamburaj and Sun[28] investigated the STL of anisotropic sandwich beams, and optimized the STL by taking the material and geometric parameters of sandwich beams as design variables. Tsai et al.[29] formulated a model for solving the composite material optimization problem in sandwich plates. Kim et al.[30] optimized the STL of honeycomb sandwich plates. Zhou et al.[31] proposed an optimization method for the dual-objective optimization of double-panel structures to minimize weight while maximizing STL. Denli and Sun[32] used a quasi-Newtonian optimization algorithm to optimize the honeycomb sandwich structure constrained by fundamental frequency and weight. Zhang et al.[33] proposed a multi-objective optimization algorithm to improve the sound insulation performance of composite laminates with viscoelastic damping layers. Jiang et al.[34] proposed a gradient sandwich plate for explosion protection, and optimized it to improve its anti-explosion performance. Dong et al.[35] presented a topology optimization scheme to design the 2D single-phase anisotropic elastic metamaterials with broadband double-negative effective material properties, and discussed the effects of several design parameters on the optimized results. Dong et al.[36] studied a porous-solid underwater metaconverter, and optimized the elastic metasurface to exhibit broadband functionalities of sound absorption and insulation. Wang et al.[37] used the genetic algorithm to study the sound absorption performance of a metamaterial structure with double-layer Nomex honeycomb, and optimized the structure. Hu et al.[38] analyzed the STL of the porous sandwich structure, and performed topology optimization.

According to the above review, sandwich plates with corrugation and auxetic honeycomb hybrid cores have special properties. Existing literature primarily focuses on the free vibration and sound insulation of composite plates, but there is limited research on the optimization for sound insulation. Considering the great influence of noise on the environment under real working conditions, it is of significance to investigate the sound insulation characteristics and optimization of hybrid sandwich panels. In this paper, the motion equation of the sandwich panel with a hybrid core is formulated based on Hamilton's variational principle, and then the sound insulation under fluid-structure coupling conditions is solved. The theoretical results are verified by COMSOL simulation results, and the effects of the structural parameters on the sound insulation are discussed. Moreover, the standard genetic algorithm is adopted to optimize the sound insulation of plates with corrugation and auxetic honeycomb hybrid cores to find the best parameter combination of the panel under certain frequency and restriction conditions.

2 Theoretical formulation

Figure 1(a) presents the model of a sandwich plate with a trapezoidal corrugation and auxetic honeycomb mixed core. A coordinate system is established on the mid-plane of the sandwich panel, where the z-axis represents the thickness direction. The upper and lower facesheets are composed of homogeneous materials, and the core layer is composed of concave auxetic hexagonal honeycomb and trapezoidal corrugation. The unit cell models of the corrugation and honeycomb are given in Fig. 1(b) and Fig. 1(c), respectively. The dimension of the panel is $a \times b$. The total thickness is h, the thicknesses of the upper and lower panels are equal and denoted by h_{f}, and the core thickness is h_{c}. The slanted side length of the honeycomb unit is l_1, and the horizontal length is l_2. The wall thickness is t_{h}. The honeycomb tilt angle is φ. The slanted side length of the corrugation unit is l_{c}, the corrugation tilt angle is θ, the platform width is d, and the corrugation thickness is t_{c}.

The relative density of the mixed core layer is represented as

$$\overline{\rho} = \overline{\rho}_{\mathrm{c}} + (1 - \overline{\rho}_{\mathrm{c}})\overline{\rho}_{\mathrm{H}}, \tag{1}$$

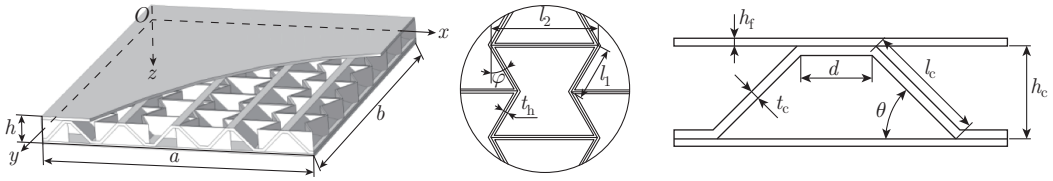

(a) Sandwich plate with corrugation-honeycomb mixed core (b) Unit cell of auxetic honeycomb (c) Unit cell of trapezoidal corrugation

Fig. 1 Model of a sandwich plate with the corrugation and auxetic honeycomb mixed core

where $\overline{\rho}_{\mathrm{c}}$ and $\overline{\rho}_{\mathrm{H}}$ represent the relative density of corrugation and honeycomb, respectively, and

$$\overline{\rho}_{\mathrm{H}} = \frac{\eta_3(\eta_1+2)}{2(\eta_1-\sin\varphi)\cos\varphi}, \quad \overline{\rho}_{\mathrm{c}} = \frac{t_{\mathrm{c}}(d+l_{\mathrm{c}})}{(d+l_{\mathrm{c}}\sin\theta)(t_{\mathrm{c}}+l_{\mathrm{c}}\cos\theta)}, \tag{2}$$

in which $\eta_1 = l_2/l_1$, and $\eta_3 = t_{\mathrm{h}}/l_1$. In the model of the sandwich plate with corrugation and auxetic honeycomb mixed core, the intermediate hybrid core layer is considered as an anisotropic homogeneous body, which can be equivalent to the one shown in Fig. 2.

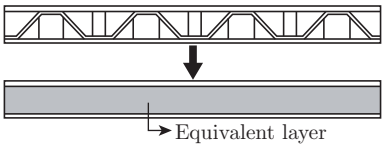

Fig. 2 Equivalent model of the corrugation and auxetic honeycomb hybrid core layer

According to the literature[9], the derived equivalent elastic parameters of the mixed core layer are represented as

$$\begin{cases} C_{11} = \dfrac{\lambda E}{1-\nu^2} + (1-\lambda)C_{11}^{\mathrm{H}}, \quad C_{22} = \dfrac{\lambda E}{1-\nu^2} + (1-\lambda)C_{22}^{\mathrm{H}}, \\ C_{12} = \dfrac{\lambda\nu E}{1-\nu^2}\dfrac{\cos\theta}{\sin\theta} + (1-\lambda)C_{12}^{\mathrm{H}}, \quad C_{44} = G\dfrac{t_{\mathrm{c}}}{l_{\mathrm{c}}}\dfrac{\sin\theta}{\cos\theta} + (1-\lambda)C_{44}^{\mathrm{H}}, \\ C_{55} = \dfrac{E}{1-\nu^2}\dfrac{t_{\mathrm{c}}}{l_{\mathrm{c}}}\sin\theta\cos\theta + (1-\lambda)C_{55}^{\mathrm{H}} \\ \qquad + \dfrac{1}{4}\dfrac{E}{1-\nu^2}\Big(\dfrac{t_{\mathrm{C}}}{l_{\mathrm{c}}}\Big)^3\Big(\dfrac{\sin^3\theta}{\cos\theta} + \dfrac{\cos^3\theta}{\sin\theta} - 2\sin\theta\cos\theta\Big), \\ C_{66} = G\dfrac{\sin\theta}{\cos\theta} + (1-\lambda)C_{66}^{\mathrm{H}}, \end{cases} \tag{3}$$

where E, ν, and G are, respectively, the elastic modulus, Poisson's ratio, and the shear modulus of the base material. λ is the volume fraction of the mixed core occupied by the corrugated component, and $\lambda = \overline{\rho}_{\mathrm{c}}$. C_{11}^{H}, C_{12}^{H}, C_{22}^{H}, C_{44}^{H}, C_{55}^{H}, and C_{66}^{H} are the elastic constants of auxetic honeycomb, and

$$\begin{aligned} C_{11}^{\mathrm{H}} = {} & E\eta_3^3(1+\eta_3^3(\tan^2\varphi+\eta_1\sec^2\varphi))\cos\varphi(\cos\varphi(\tan^2\varphi+\eta_3^2)(\eta_1-\sin\varphi) \\ & \cdot(1+\eta_3^3(\tan^2\varphi+\eta_1\sec^2\varphi)) - (1-\eta_3^2)^2(\eta_1-\sin\varphi)\sin^2\varphi)^{-1}, \end{aligned} \tag{4a}$$

$$C_{22}^{\mathrm{H}} = \frac{E\eta_3^3(\eta_1-\sin\varphi)(\tan^2\varphi+\eta_3^2)}{\cos^3\varphi(1+\eta_3^3(\tan^2\varphi+\eta_1\sec^2\varphi))(\tan^2\varphi+\eta_3^2) - (1-\eta_3^2)^2\sin^2\varphi\cos\varphi}, \tag{4b}$$

$$C_{12}^{\mathrm{H}}=\frac{E\eta_3^3(1-\eta_3^2)\sin\varphi}{\cos^3\varphi(1+\eta_3^3(\tan^2\theta+\eta_1\sec^2\varphi))(\tan^2\varphi+\eta_3^2)-(1-\eta_3^2)^2\sin^2\varphi\cos\varphi}, \tag{4c}$$

$$C_{44}^{\mathrm{H}}=G\frac{\eta_3}{2\cos\varphi}\Big(\frac{\eta_1-\sin\varphi}{1+2\eta_1}+\frac{\eta_1+2\sin^2\varphi}{2(\eta_1-\sin\varphi)}\Big), \tag{4d}$$

$$C_{55}^{\mathrm{H}}=G\frac{\eta_3\cos\varphi}{\eta_1-\sin\varphi},\quad C_{66}^{\mathrm{H}}=\frac{E\eta_3^3}{\eta_1(1+2\eta_1)\cos\varphi}. \tag{4e}$$

2.1 Dynamic equations

According to the third-order shear deformation theory (TSDT)[39], the displacement field can be expressed as

$$\begin{cases} u(x,y,z,t)=u_0+z\phi_x-\dfrac{4z^3}{3h^2}\Big(\phi_x+\dfrac{\partial w_0}{\partial x}\Big),\\ v(x,y,z,t)=v_0+z\phi_y-\dfrac{4z^3}{3h^2}\Big(\phi_y+\dfrac{\partial w_0}{\partial y}\Big),\quad w(x,y,z,t)=w_0, \end{cases} \tag{5}$$

where u_0, v_0, w_0 and ϕ_x, ϕ_y are the displacements of any point on the midplane and the rotations, respectively. Compared with the first-order shear deformation theory (FSDT), the TSDT can avoid the selection of the shear correction factors, and satisfy the zero traction on the top and bottom surfaces of the sandwich plate.

According to the assumptions of small deformations, the strain-displacement relation is

$$\begin{cases} \varepsilon_{xx}=\dfrac{\partial u}{\partial x},\quad \varepsilon_{yy}=\dfrac{\partial v}{\partial y},\quad \gamma_{xy}=\dfrac{\partial u}{\partial y}+\dfrac{\partial v}{\partial x},\\ \varepsilon_{zz}=\dfrac{\partial w}{\partial z},\quad \gamma_{xz}=\dfrac{\partial u}{\partial z}+\dfrac{\partial w}{\partial x},\quad \gamma_{yz}=\dfrac{\partial v}{\partial z}+\dfrac{\partial w}{\partial y}. \end{cases} \tag{6}$$

The linear constitutive relation of the sandwich plate is

$$\begin{pmatrix}\sigma_{xx}^{(k)}\\ \sigma_{yy}^{(k)}\\ \tau_{yz}^{(k)}\\ \tau_{xz}^{(k)}\\ \tau_{xy}^{(k)}\end{pmatrix}=\begin{pmatrix}C_{11}^{(k)} & C_{12}^{(k)} & 0 & 0 & 0\\ C_{21}^{(k)} & C_{22}^{(k)} & 0 & 0 & 0\\ 0 & 0 & C_{44}^{(k)} & 0 & 0\\ 0 & 0 & 0 & C_{55}^{(k)} & 0\\ 0 & 0 & 0 & 0 & C_{66}^{(k)}\end{pmatrix}\begin{pmatrix}\varepsilon_{xx}^{(k)}\\ \varepsilon_{yy}^{(k)}\\ \gamma_{yz}^{(k)}\\ \gamma_{xz}^{(k)}\\ \gamma_{xy}^{(k)}\end{pmatrix}, \tag{7}$$

where $k=1$ and $k=3$ represent the upper and lower layers, respectively, and their corresponding elastic constants are $C_{11}=C_{22}=E/(1-\nu^2)$, $C_{12}=C_{21}=E\nu/(1-\nu^2)$, and $C_{44}=C_{55}=C_{66}=G=E/2(1+\nu)$; $k=2$ represents the hybrid core layer.

According to the Hamiltonian variational principle[39], the kinematic equation of the sandwich plate with a hybrid core is obtained as

$$\frac{\partial N_{xx}}{\partial x}+\frac{\partial N_{xy}}{\partial y}=I_0\frac{\partial^2 u_0}{\partial t^2}-I_1\frac{\partial}{\partial x}\Big(\frac{\partial^2 w_0}{\partial t^2}\Big)+J_1\frac{\partial^2\phi_x}{\partial t^2}, \tag{8a}$$

$$\frac{\partial N_{yy}}{\partial y}+\frac{\partial N_{xy}}{\partial x}=I_0\frac{\partial^2 v_0}{\partial t^2}-I_1\frac{\partial}{\partial y}\Big(\frac{\partial^2 u_0}{\partial t^2}\Big)+J_1\frac{\partial^2\phi_y}{\partial t^2}, \tag{8b}$$

$$\begin{aligned}&\frac{\partial^2 M_{xx}}{\partial x^2}+\frac{\partial^2 M_{xy}}{\partial x\partial y}+\frac{\partial^2 M_{yy}}{\partial y^2}-q=I_0\frac{\partial^2 w_0}{\partial t^2}+I_1\frac{\partial}{\partial x}\Big(\frac{\partial^2 u_0}{\partial t^2}\Big)+I_1\frac{\partial}{\partial y}\Big(\frac{\partial^2 v_0}{\partial t^2}\Big)\\ &-I_2\frac{\partial^2}{\partial x^2}\Big(\frac{\partial^2 w_0}{\partial t^2}\Big)-I_2\frac{\partial^2}{\partial y^2}\Big(\frac{\partial^2 w_0}{\partial t^2}\Big)+K_2\frac{\partial^2}{\partial x^2}\Big(\frac{\partial^2\phi_x}{\partial t^2}\Big)+K_2\frac{\partial^2}{\partial y^2}\Big(\frac{\partial^2\phi_y}{\partial t^2}\Big),\end{aligned} \tag{8c}$$

$$\frac{\partial M_{xx}}{\partial x}+\frac{\partial M_{xy}}{\partial y}-Q_x=J_1\frac{\partial^2 u_0}{\partial t^2}-K_2\frac{\partial}{\partial x}\Big(\frac{\partial^2 w_0}{\partial t^2}\Big)+J_2\frac{\partial^2\phi_x}{\partial t^2}, \tag{8d}$$

$$\frac{\partial M_{yy}}{\partial y}+\frac{\partial M_{xy}}{\partial x}-Q_y=J_1\frac{\partial^2 v_0}{\partial t^2}-K_2\frac{\partial}{\partial y}\Big(\frac{\partial^2 w_0}{\partial t^2}\Big)+J_2\Big(\frac{\partial^2\phi_y}{\partial t^2}\Big), \tag{8e}$$

where

$$\begin{cases}\begin{pmatrix}N_{\xi\eta}\\M_{\xi\eta}\\H_{\xi\eta}\end{pmatrix}=\int_{-\frac{h}{2}}^{\frac{h}{2}}\sigma_{\xi\eta}\begin{pmatrix}1\\z\\f\end{pmatrix}\mathrm{d}z,\quad Q_\xi=\int_{-\frac{h}{2}}^{\frac{h}{2}}\sigma_{\xi z}f'\mathrm{d}z,\quad \xi,\eta=x,y,\\(I_0,I_1,I_2,J_1,J_2,K_2)=\int_{-\frac{h}{2}}^{\frac{h}{2}}\rho(1,z,z^2,f,f^2,zf)\mathrm{d}z,\end{cases} \tag{9}$$

q is the external load, and ρ is the density of the material.

Substituting Eqs. (5)–(7) into Eq. (8) yields

$$\begin{aligned}&\Big(A_{11}\frac{\partial^2}{\partial x^2}+A_{66}\frac{\partial^2}{\partial y^2}-I_0\frac{\partial^2}{\partial t^2}\Big)u_0+\Big(B_{11}\frac{\partial^3}{\partial x^3}+B_{21}\frac{\partial^3}{\partial x\partial y^2}+2B_{66}\frac{\partial^3}{\partial x\partial y^2}-I_1\frac{\partial^3}{\partial x\partial t^2}\Big)w_0\\&+\Big(A_{21}\frac{\partial^2}{\partial x\partial y}+A_{66}\frac{\partial^2}{\partial x\partial y}\Big)v_0+\Big(D_{11}\frac{\partial^2}{\partial x^2}+D_{66}\frac{\partial^2}{\partial y^2}-J_1\frac{\partial^2}{\partial t^2}\Big)\phi_x\\&+\Big(D_{21}\frac{\partial^2}{\partial x\partial y}+D_{66}\frac{\partial^2}{\partial x\partial y}\Big)\phi_y=0,\end{aligned} \tag{10a}$$

$$\begin{aligned}&\Big(A_{21}\frac{\partial^2}{\partial x\partial y}+A_{66}\frac{\partial^2}{\partial x\partial y}\Big)u_0+\Big(-B_{22}\frac{\partial^3}{\partial x^3}-B_{21}\frac{\partial^3}{\partial x^2\partial y}-2B_{66}\frac{\partial^3}{\partial x^2\partial y}+I_1\frac{\partial^3}{\partial y\partial t^2}\Big)w_0\\&+\Big(A_{22}\frac{\partial^2}{\partial y^2}+A_{66}\frac{\partial^2}{\partial x^2}-I_0\frac{\partial^2}{\partial t^2}\Big)v_0+\Big(D_{21}\frac{\partial^2}{\partial x\partial y}+D_{66}\frac{\partial^2}{\partial x\partial y}\Big)\phi_x\\&+\Big(D_{22}\frac{\partial^2}{\partial y^2}+D_{66}\frac{\partial^2}{\partial x^2}-J_1\frac{\partial^2}{\partial t^2}\Big)\phi_y=0,\end{aligned} \tag{10b}$$

$$\begin{aligned}&\Big(B_{11}\frac{\partial^3}{\partial x^3}+B_{21}\frac{\partial^3}{\partial x\partial y^2}+2B_{66}\frac{\partial^3}{\partial x\partial y^2}-I_1\frac{\partial^3}{\partial x\partial t^2}\Big)u_0\\&+\Big(-B_{22}\frac{\partial^3}{\partial y^3}-B_{21}\frac{\partial^3}{\partial x^2\partial y}-2B_{66}\frac{\partial^3}{\partial x^2\partial y}+I_1\frac{\partial^3}{\partial y\partial t^2}\Big)v_0\\&+\Big(-G_{11}\frac{\partial^4}{\partial x^4}-G_{21}\frac{\partial^4}{\partial x^2\partial y^2}-G_{12}\frac{\partial^4}{\partial x^2\partial y^2}-4G_{66}\frac{\partial^4}{\partial x^2\partial y^2}-G_{22}\frac{\partial^4}{\partial y^4}+I_2\frac{\partial^2}{\partial x^2}+I_2\frac{\partial^2}{\partial y^2}\Big)w_0\\&+\Big(L_{11}\frac{\partial^3}{\partial x^3}+L_{21}\frac{\partial^3}{\partial x\partial y^2}+2B_{66}\frac{\partial^3}{\partial x\partial y^2}-K_2\frac{\partial^3}{\partial x\partial t^2}\Big)\phi_x\\&+\Big(L_{22}\frac{\partial^3}{\partial y^3}+L_{21}\frac{\partial^3}{\partial x^2\partial y}+2L_{66}\frac{\partial^3}{\partial x^2\partial y}-K_2\frac{\partial^3}{\partial y\partial t^2}\Big)\phi_y-q=0,\end{aligned} \tag{10c}$$

$$\begin{aligned}&\Big(D_{11}\frac{\partial^2}{\partial x^2}+D_{66}\frac{\partial^2}{\partial y^2}-J_1\frac{\partial^2}{\partial t^2}\Big)u_0+\Big(L_{11}\frac{\partial^3}{\partial x^3}+L_{21}\frac{\partial^3}{\partial x\partial y^2}+2B_{66}\frac{\partial^3}{\partial x\partial y^2}-K_2\frac{\partial^3}{\partial x\partial t^2}\Big)w_0\\&+\Big(D_{21}\frac{\partial^2}{\partial x\partial y}+D_{66}\frac{\partial^2}{\partial x\partial y}\Big)v_0+\Big(R_{11}\frac{\partial^2}{\partial x^2}+R_{66}\frac{\partial^2}{\partial y^2}+V_{55}-J_2\frac{\partial^2}{\partial t^2}\Big)\phi_x\\&+\Big(R_{21}\frac{\partial^2}{\partial x\partial y}+R_{66}\frac{\partial^2}{\partial x\partial y}\Big)\phi_y=0,\end{aligned} \tag{10d}$$

$$\Big(D_{21}\frac{\partial^2}{\partial x\partial y}+D_{66}\frac{\partial^2}{\partial x\partial y}\Big)u_0+\Big(L_{22}\frac{\partial^3}{\partial x^3}+L_{21}\frac{\partial^3}{\partial x^2\partial y}+2L_{66}\frac{\partial^3}{\partial x^2\partial y}-K_2\frac{\partial^3}{\partial y\partial t^2}\Big)w_0$$

$$+\Big(D_{22}\frac{\partial^2}{\partial y^2}+D_{66}\frac{\partial^2}{\partial x^2}-J_1\frac{\partial^2}{\partial t^2}\Big)v_0+\Big(R_{21}\frac{\partial^2}{\partial x\partial y}+R_{66}\frac{\partial^2}{\partial x\partial y}\Big)\phi_x$$
$$+\Big(R_{22}\frac{\partial^2}{\partial y^2}+R_{66}\frac{\partial^2}{\partial x^2}+V_{44}-J_2\frac{\partial^2}{\partial t^2}\Big)\phi_y=0, \tag{10e}$$

where

$$(A_{ij},B_{ij},D_{ij},G_{ij},L_{ij},R_{ij},V_{ij})=\sum_{k=1}^{3}\int_{\zeta_k}^{\zeta_{k+1}}C_{ij}^{(k)}(1,z,f,z^2,zf,f^2,(f')^2)\mathrm{d}z. \tag{11}$$

The displacement components for the simply supported edges are expanded as

$$\begin{cases}u_0=\displaystyle\sum_{m=1}^{\infty}\sum_{n=1}^{\infty}U_{mn}\cos\Big(\frac{m\pi x}{a}\Big)\sin\Big(\frac{n\pi y}{b}\Big)\mathrm{e}^{\mathrm{i}\omega t},\\ v_0=\displaystyle\sum_{m=1}^{\infty}\sum_{n=1}^{\infty}V_{mn}\sin\Big(\frac{m\pi x}{a}\Big)\cos\Big(\frac{n\pi y}{b}\Big)\mathrm{e}^{\mathrm{i}\omega t},\\ w_0=\displaystyle\sum_{m=1}^{\infty}\sum_{n=1}^{\infty}W_{mn}\sin\Big(\frac{m\pi x}{a}\Big)\sin\Big(\frac{n\pi y}{b}\Big)\mathrm{e}^{\mathrm{i}\omega t},\\ \phi_x=\displaystyle\sum_{m=1}^{\infty}\sum_{n=1}^{\infty}\Phi_{xmn}\cos\Big(\frac{m\pi x}{a}\Big)\sin\Big(\frac{n\pi y}{b}\Big)\mathrm{e}^{\mathrm{i}\omega t},\\ \phi_y=\displaystyle\sum_{m=1}^{\infty}\sum_{n=1}^{\infty}\Phi_{ymn}\sin\Big(\frac{m\pi x}{a}\Big)\cos\Big(\frac{n\pi y}{b}\Big)\mathrm{e}^{\mathrm{i}\omega t},\end{cases} \tag{12}$$

in which $\mathrm{i}=\sqrt{-1}$, m and n are the half-wave numbers, and ω is the circular frequency.

Substituting Eq. (12) into Eq. (10) yields

$$(\boldsymbol{K}-\omega^2\boldsymbol{M})(\boldsymbol{\delta})=\boldsymbol{F}, \tag{13}$$

where $\boldsymbol{K}$ is the structural stiffness matrix, $\boldsymbol{M}$ is the mass matrix, $\boldsymbol{F}$ is the external force matrix, and $(\boldsymbol{\delta})^{\mathrm{T}}=(U_{mn},V_{mn},W_{mn},\Phi_{xmn},\Phi_{ymn})$ is the amplitude of the displacement field. If the external force is ignored, the natural frequencies of the free vibration can be obtained.

2.2 Sound insulation

Figure 3 gives the harmonic acoustic wave P incident on the upper surface of the plate, where ψ_1 is the incident angle, and ψ_2 is the azimuth angle. The incident sound pressure is expressed by

$$p_{\mathrm{i}}(x,y,z,t)=p_0\mathrm{e}^{\mathrm{i}(\omega t-k_xx-k_yy-k_zz)}, \tag{14}$$

where p_0 is the amplitude, and the wave numbers k_x, k_y, and k_z are represented as $k_x=\frac{\omega}{c}\sin\psi_1\cos\psi_2$, $k_y=\frac{\omega}{c}\sin\psi_1\sin\psi_2$, and $k_z=\frac{\omega}{c}\cos\psi_1$, and c is the acoustic speed.

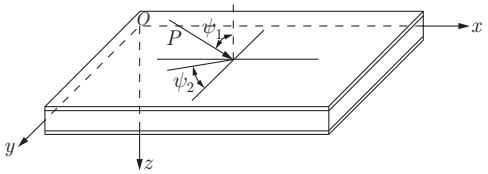

Fig. 3 Plane sound wave incident on the sandwich plate

Accordingly, the reflected and transmitted sound pressures can be assumed as

$$\begin{cases} p_{\mathrm{r}}(x,y,t) = \displaystyle\sum_{m=1}^{\infty}\sum_{n=1}^{\infty} R_{mn}\sin\frac{m\pi x}{a}\sin\frac{n\pi y}{b}\mathrm{e}^{\mathrm{i}(\omega t+k_z z)}, \\ p_{\mathrm{t}}(x,y,t) = \displaystyle\sum_{m=1}^{\infty}\sum_{n=1}^{\infty} T_{mn}\sin\frac{m\pi x}{a}\sin\frac{n\pi y}{b}\mathrm{e}^{\mathrm{i}(\omega t-k_z z)}, \end{cases} \tag{15}$$

where T_{mn} and R_{mn} are, respectively, the amplitudes of the transmitted sound pressure and the reflected sound pressure.

Under the excitation of the sound pressure, the external force is represented as

$$q = p_{\mathrm{t}}\Big(x,y,\frac{h}{2},t\Big) - p_{\mathrm{i}}\Big(x,y,-\frac{h}{2},t\Big) - p_{\mathrm{r}}\Big(x,y,-\frac{h}{2},t\Big). \tag{16}$$

The fluid-solid coupling conditions at the interface are

$$z=\frac{h}{2}:\frac{\partial p_{\mathrm{t}}}{\partial z}=\rho_0\omega^2 w, \quad z=-\frac{h}{2}:\frac{\partial(p_{\mathrm{i}}+p_{\mathrm{r}})}{\partial z}=\rho_0\omega^2 w, \tag{17}$$

where ρ_0 is the density of the air. Assume that the incident and transmitted sound power are

$$W_{\mathrm{i}}=\frac{1}{2\rho_0 c}\iint |p_{\mathrm{i}}|^2\mathrm{d}A, \quad W_{\mathrm{t}}=\frac{1}{2\rho_0 c}\iint |p_{\mathrm{t}}|^2\mathrm{d}A. \tag{18}$$

Then, the sound insulation is defined as

$$L_{\mathrm{STL}} = 10\lg\Big(\frac{W_{\mathrm{i}}}{W_{\mathrm{t}}}\Big). \tag{19}$$

3 Results and discussion

In this section, the sound insulation of the sandwich plates with a corrugation and auxetic honeycomb hybrid core is analyzed. In the calculations, the geometrical parameters are: $a = 320\,\mathrm{mm}$, $b = 259.8\,\mathrm{mm}$, $h_{\mathrm{f}} = 1\,\mathrm{mm}$, $h_{\mathrm{c}} = 8\,\mathrm{mm}$, $l_1 = 10\,\mathrm{mm}$, $l_2 = 20\,\mathrm{mm}$, $t_{\mathrm{h}} = 1\,\mathrm{mm}$, $\varphi = 30^\circ$, $l_{\mathrm{c}} = 10\,\mathrm{mm}$, $\theta = 45^\circ$, $d = 3\,\mathrm{mm}$, and $t_{\mathrm{c}} = 1\,\mathrm{mm}$. The base material made of the sandwich plates is aluminum with properties: $E = 70\,\mathrm{Pa}$, $\nu = 0.3$, and $\rho = 2\,700\,\mathrm{kg/m^3}$. The acoustic speed is $c = 340\,\mathrm{m/s}$, the air density is $\rho_0 = 1.293\,\mathrm{kg/m^3}$, $\psi_1 = 0^\circ$, $\psi_2 = 0^\circ$, and $P_0 = 1\,\mathrm{Pa}$.

To prove the accuracy of the established STL theoretical model, validation is performed using COMSOL. In the simulation, the acoustic module is selected. First, the equivalent solid model is created, and then the cavities on the upper and lower surfaces of the solid model are established. Second, the material parameters are assigned. The boundary conditions are achieved by applying translational and rotational displacements on all four edges. The quadrilateral mesh is used for discretization. By the solution in the frequency domain, the STL curve can be obtained. The pressure acoustics module is used to simulate two air cavities on the top and bottom panels of the structure with a corrugation and auxetic honeycomb hybrid core in the "solid mechanics" module. After setting specific parameters and applying a given sound wave, the STL curve is calculated. The theoretical results and finite element (FE) simulation results are both depicted in Fig. 4(a). It is observable that except for some differences at lower frequencies, the STL curve calculated from the theoretical model in this paper matches well with the one obtained from the FE simulation, which verifies the accuracy of the theoretical model. In the theoretical calculations, the STL curves are calculated for frequencies of 500 Hz, 1 500 Hz, and 3 500 Hz, as shown in Fig. 4(b). We can see that for the given three frequencies, the STL curves converge well when $m = n = 40$, which will be used in the subsequent sound insulation calculations.

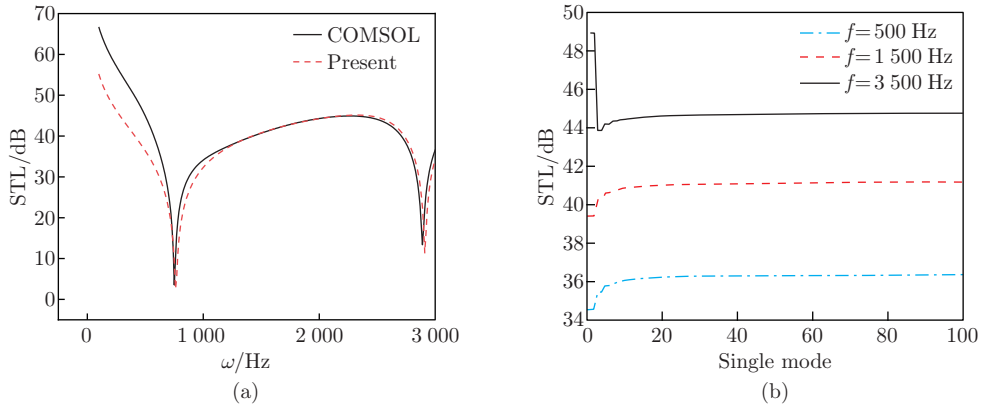

Fig. 4 (a) Present theoretical and COMSOL simulation results of STL. (b) STL convergence (color online)

For comparisons, the natural frequencies of the sandwich plate under the same conditions are listed in Table 1. From Fig. 4(a) and Table 1, we find that there are two troughs on the STL curves. The frequency at the first trough is close to the first-order natural frequency of the system, and the frequency at the second trough is close to the fourth- or fifth-order natural frequency, indicating that the structure resonates at the frequencies corresponding to the troughs, which leads to a significant increase in the transmitted sound energy. Thus, the sound insulation performance for the entire structure rapidly decreases near the resonance frequency, and a sound trough occurs. However, the vertically incident sound wave cannot fully excite all vibration modes of the entire sandwich plate structure. Therefore, there are no corresponding troughs on the STL curve near certain natural frequencies.

Table 1 Natural frequencies of the sandwich plate with the corrugation and auxetic honeycomb hybrid core

Method	ω_1/Hz	ω_2/Hz	ω_3/Hz	ω_4/Hz	ω_5/Hz	ω_6/Hz
Present	755.1	1 606.4	1 979.1	2 907.9	2 910.1	3 878.4
COMSOL	757.2	1 611.1	1 983.1	2 914.9	2 917.0	3 879.3

In order to better illustrate the relationship between the vibration modes and STL, the vibration modes of the sandwich plate under the excited sound pressure are shown in Fig. 5, and the vibration modes for the corresponding free vibration of the structure are given in Fig. 6. By comparisons, we can find that the vibration modes at 755 Hz and 2 910 Hz in Fig. 5 are basically consistent with the first vibration mode and the fifth vibration mode in Fig. 6, respectively. This shows that resonances occur at these corresponding frequencies, and the acoustic wave is easily transmitted through the structure.

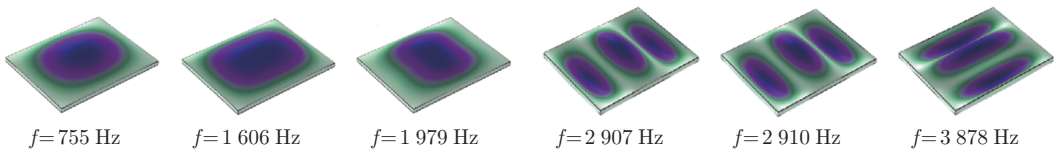

Fig. 5 Vibration modes of the sandwich plate under the excited sound pressure (color online)

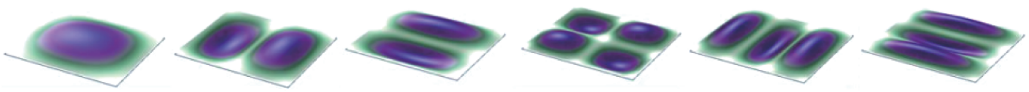

Fig. 6 Vibration modes for the free vibration of the sandwich plate (color online)

The core layer is integrally connected with the upper and lower panels in the sandwich structure, and thus its thickness will affect the structural properties. When the total thickness remains unchanged, only the core thickness is changed, namely $h_c = 3\,\text{mm}$, $6\,\text{mm}$, and $9\,\text{mm}$. The thicknesses of the upper and lower panels change accordingly. The calculated STL curves of the sandwich plate are illustrated in Fig. 7(a). It is observed that with the increase in the core thickness, the troughs on the STL curves move towards high frequencies, which is consistent with the influence of the core thickness on the fundamental frequency in Fig. 7(b). As the core thickness increases, the STL curve gradually decreases, and the sound insulation performance gradually decreases. It can also be clearly seen from the contour map that the STL is larger when the core thickness is smaller in the range of 1 000 Hz–2 500 Hz.

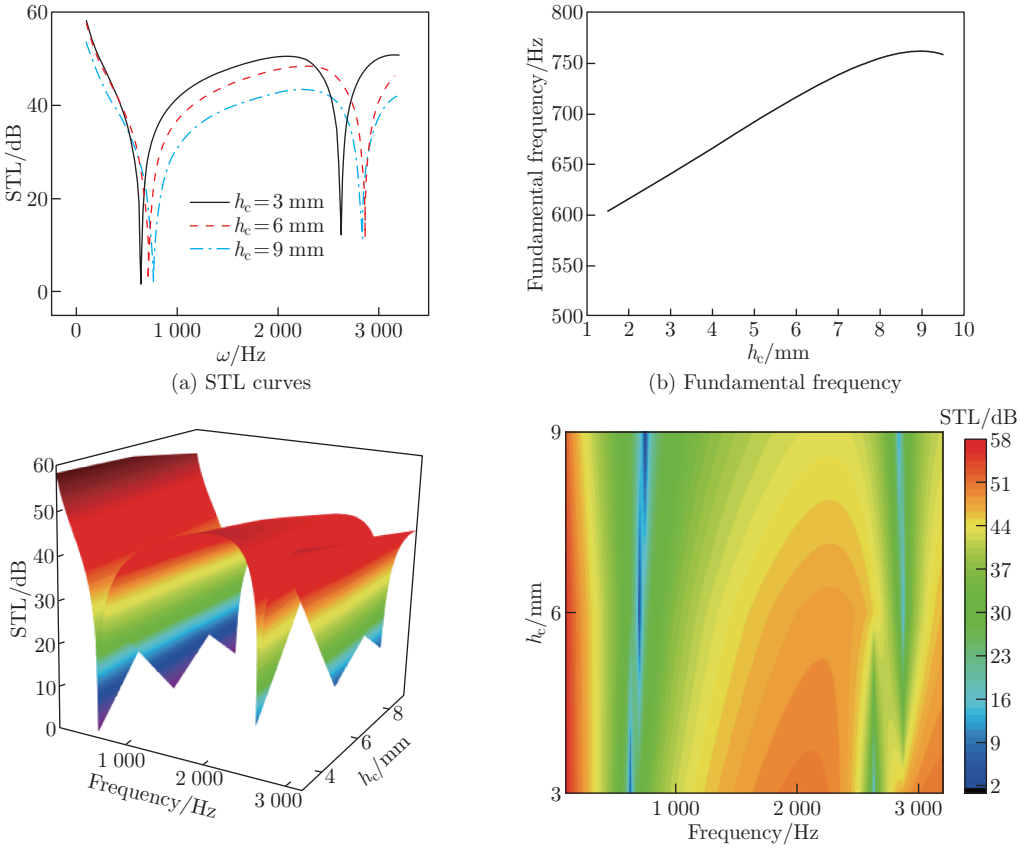

(a) STL curves

(b) Fundamental frequency

(c) 3D STL curves and its contour maps under various h_c

Fig. 7 Effects of the core thicknesses h_c on the STL (color online)

Figure 8 indicates the effects of the honeycomb wall thickness t_h on the sound insulation performance of the sandwich structure with the mixed core, where we take t_h as 1 mm, 2 mm, and 3 mm, and other parameters remain unchanged. It is observed that when t_h increases, the troughs on the STL curves shift towards low frequencies, and this change is more pronounced at higher frequencies. In other words, the decrease in the distance between troughs leads to more troughs within a certain frequency range. This is because when only t_h is changed, the proportion of aluminum in the honeycomb structure increases, which makes the structure more similar to a solid aluminum plate. The natural frequency of a solid aluminum plate is lower than that of the same-sized mixed core layer. The change of the trough is also consistent with that of the fundamental frequency in Fig. 8(b). As t_h increases, the STL curve gradually rises,

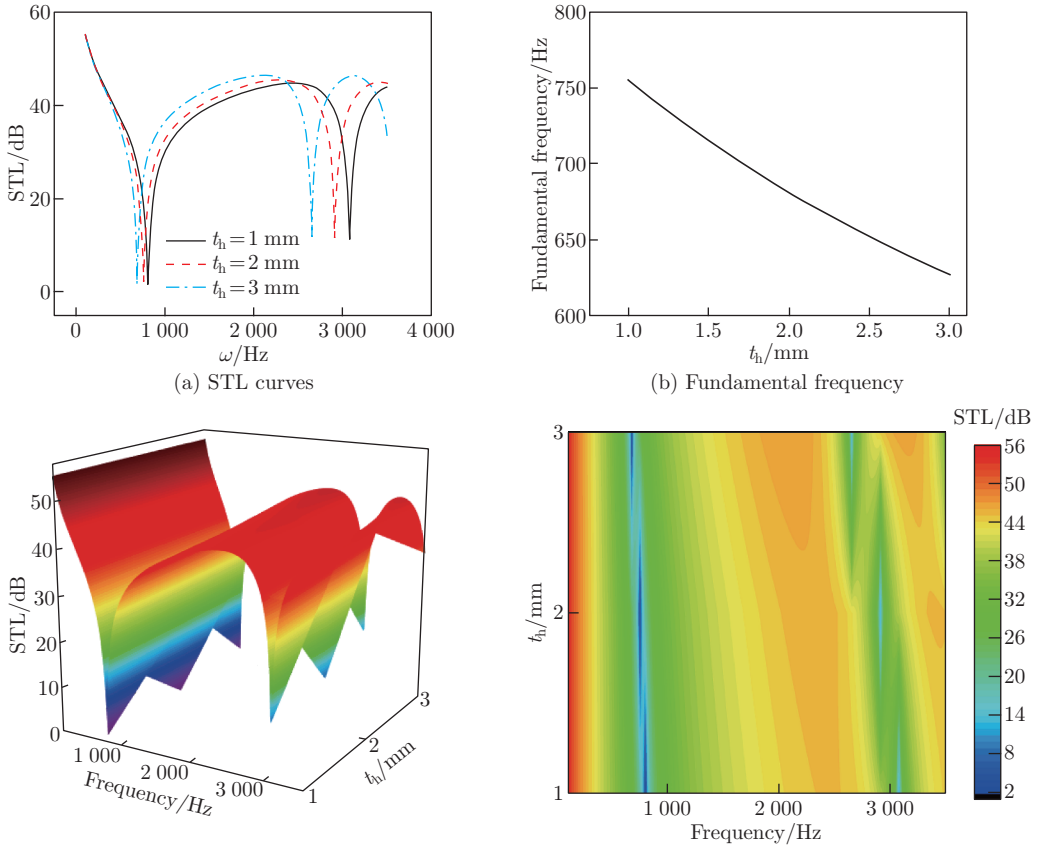

(a) STL curves

(b) Fundamental frequency

(c) 3D STL curves and its contour maps under various t_h

Fig. 8 Effects of the honeycomb wall thicknesses t_h on the STL (color online)

improving the sound insulation performance. Additionally, the STL at high-frequency troughs is larger than that at low-frequency troughs, indicating better sound insulation performance at higher frequencies. From the contour map, it is seen that the STL is relatively high at extremely low frequencies, and no wave trough appears within the range of 1 000 Hz to 2 500 Hz.

Finally, the effects of the corrugated wall thickness on the STL of the sandwich plate with the corrugation and auxetic honeycomb hybrid core are studied. While keeping the other geometric parameters constant and only varying the corrugated wall thickness (t_c = 0.5 mm, 1.5 mm, and 3 mm), the STL curves and contour maps are shown in Fig. 9. From the figure, it is observed that with the increase in t_c, same to the change trend of the natural frequency with the corrugated wall thickness given in Fig. 9(b), the STL troughs move towards low frequencies. Similar to the case of changing the honeycomb wall thickness, when only t_c is changed, the proportion of aluminum material in the sandwich panel increases, resulting in a significant increase in the overall structural mass, and thus the natural frequency decreases. With the increase in t_c, the STL curve shows a slight increase, indicating an improvement in the sound insulation performance. The contour map of sound insulation also reveals that the sound insulation troughs clearly shift towards lower frequencies.

4 Optimization for sound insulation

Many practical application problems are complex, which involve multiple optimization variables and constraints, and traditional optimization methods struggle to efficiently handle such

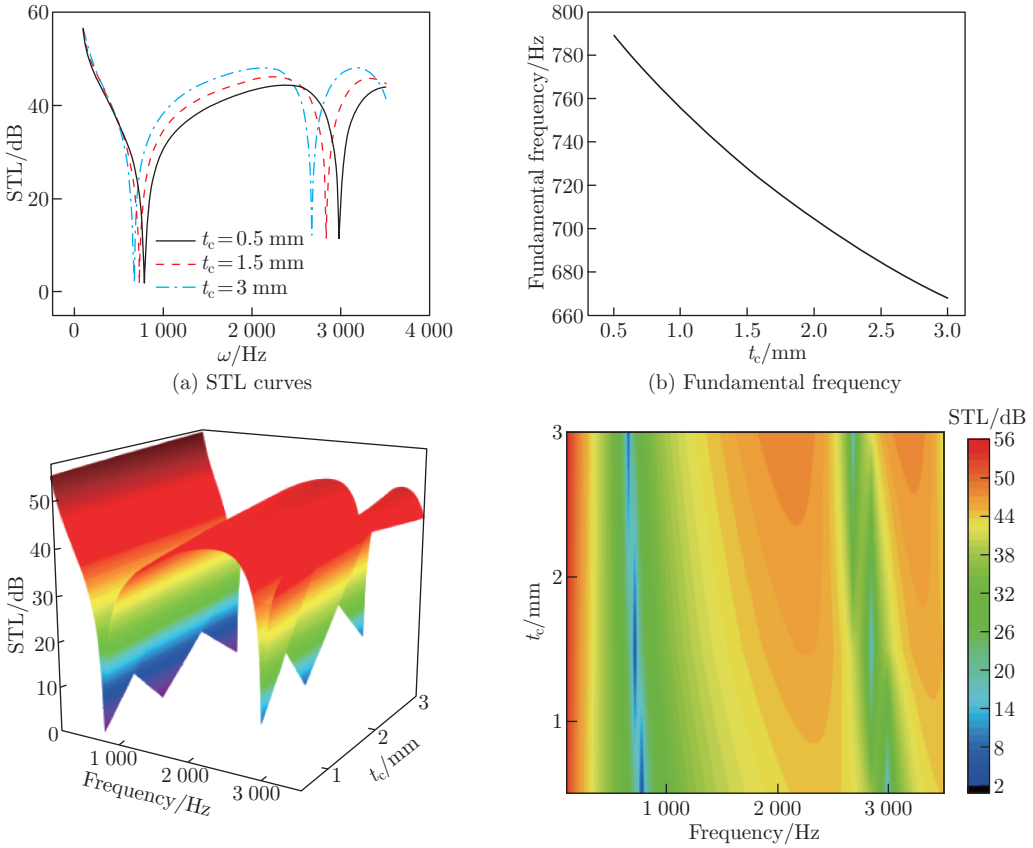

(a) STL curves

(b) Fundamental frequency

(c) 3D STL curves and its contour maps under various t_c

Fig. 9 Effects of t_c on the STL (color online)

problems. The widely used genetic algorithm is a type of evolutionary computation algorithm specifically designed to handle these complex problems. Here, we will adopt it to optimize the sandwich plate with a mixed core.

To optimize the design of the sandwich plate and maximize the STL (L_{STL}) under certain conditions to achieve the best sound insulation effect, the optimization problem is formulated as

$$\max f(x) = L_{\mathrm{STL}}(x), \quad x = (x_1, x_2, x_3, \cdots x_n) \quad \text{s.t.} \quad x \in \mathbf{R}^n, \tag{20}$$

where $f(x)$ represents the objective function, the variable x represents the parameters involved in the optimization, encompassing various design variables.

4.1 Optimization of single parameter

The sum of the STL at 500 Hz, 1 000 Hz, and 2 000 Hz is taken as the objective function, the total thickness is kept constant as 10 mm, and the core thickness h_c is taken as the only design variable within the range of 2 mm $\leqslant h_c \leqslant$ 9 mm. The objective function is expressed as

$$\max f(x) = \frac{1}{3}(L_{\mathrm{STL},500}(x) + L_{\mathrm{STL},1\,000}(x) + L_{\mathrm{STL},2\,000}(x)). \tag{21}$$

The population size is set to 10, with 30 optimization generations and a chromosome length of 10. The final optimized population distribution, the change trend of the best individuals, and the optimized STL curves are shown in Fig. 10.

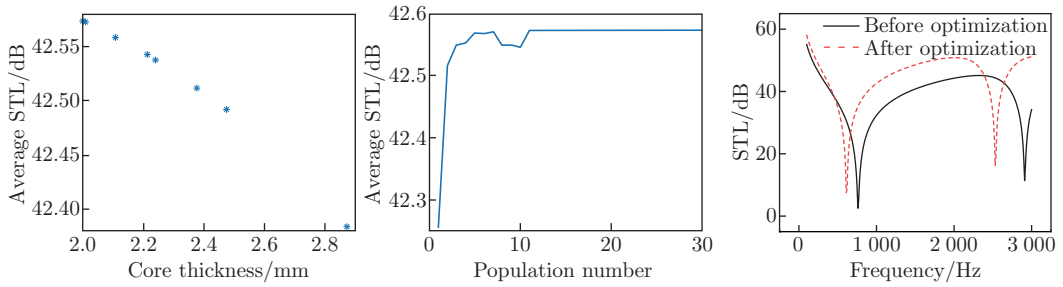

(a) Final population distribution (b) Optimal individual change trend (c) Optimized STL comparison

Fig. 10 Optimized results of the core thickness at multiple frequencies (color online)

From the figure, we find that the optimal individual in the final population is 2 mm, and the majority of the final population is concentrated in the range of 2 mm to 2.9 mm, with the STL value converging at 42.554 dB. This corresponds to the previous research indicated in Fig. 7, where the STL gradually decreases with the increase in the core thickness. Therefore, as the core thickness is minimal, the STL value of the sandwich plate with the hybrid core is maximized, achieving the best sound insulation effect. After optimization, the increases in the STL values at 500 Hz, 1 000 Hz, and 2 000 Hz are, respectively, $\Delta L_{\mathrm{STL},500} = -2.6\,\mathrm{dB}$, $\Delta L_{\mathrm{STL},1\,000} = 10.3\,\mathrm{dB}$, and $\Delta L_{\mathrm{STL},2\,000} = 7.0\,\mathrm{dB}$.

In the case of a fixed perimeter, the aspect ratio a/b is taken as the independent variable satisfying $a + b = 0.58\,\mathrm{m}$, and the length a of the plate is in the range of $0.1\,\mathrm{m} \leqslant a \leqslant 0.48\,\mathrm{m}$. Under the excitation of the sound pressure with 1 000 Hz, the STL is taken as the objective function $\max f(x) = L_{\mathrm{STL},1\,000}(x)$.

By taking the population number as 10, the number of optimization generations as 30, and the chromosome length as 10, the final optimized population distribution, the change trend of optimal individuals, and the optimized STL curve are illustrated in Fig. 11. We see that the optimal individual result of the final population is $a = 1\,\mathrm{mm}$, i.e., when $a/b = 0.208$, the STL value at 1 000 Hz is the largest, and the STL value converges at 57 dB. As can be seen from the figure, the first trough on the optimized STL curve appears at about 3 000 Hz, which is because under the condition of simply supported structure with a certain circumference, when a/b is larger or smaller, the structural stiffness will be greatly strengthened, resulting in a substantial increase in the fundamental frequency, and the optimal result appears at the minimum of a/b. In addition, the sound insulation at 1 000 Hz is greatly increased when a/b is minimum, and the optimized STL is increased by 24.9 dB.

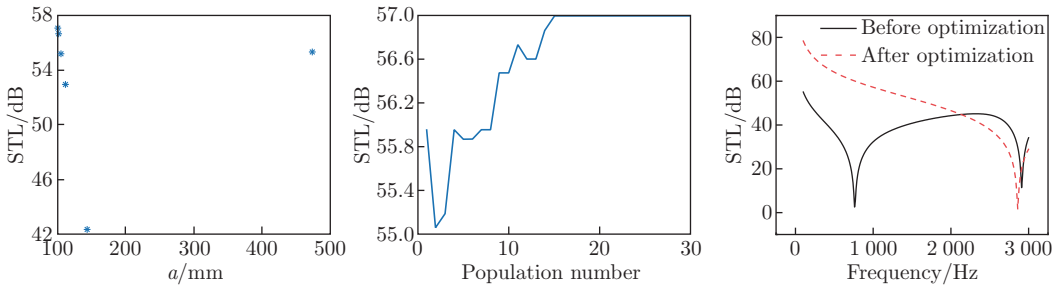

(a) Final population distribution (b) Optimal individual change trend (c) Optimized STL comparison

Fig. 11 Optimized results of the aspect ratio (color online)

4.2 Dual-parameter optimization

Since the optimization involves multiple parameters, in order to increase the search efficiency, the population number is set to 15, the number of optimization generations is set to 30, and the

chromosome length is set to 10. The change trend of the optimal individual and the optimized STL curve are shown in Fig. 12. It can be seen that when the number of optimization generations is 20, the optimization result has converged. After optimization, the optimal individual is $h_c = 5.83\,\text{mm}$, $a = 0.114\,\text{m}$, the STL value converges at 61.5 dB, and $\Delta L_{\text{STL}} = 29.33\,\text{dB}$. From the STL comparison diagram before and after optimization, we find that when two design variables are involved in optimization, the optimized STL curve at 1 000 Hz is improved to a certain extent compared with that of no optimization or the optimization with a single design variable, which increases the sound insulation effect.

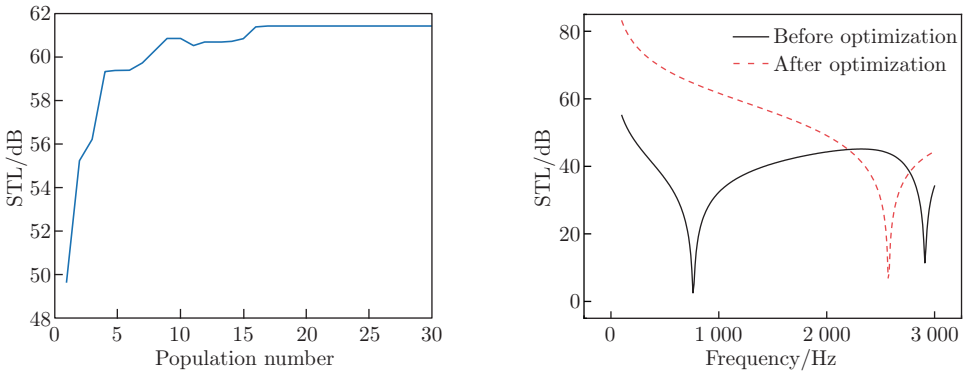

(a) Optimal individual change trend (b) Optimized STL comparison

Fig. 12 Dual-parameter optimized results of the core thickness-to-aspect ratio (color online)

4.3 Comprehensive optimization

Combining the optimizations above, the multiple parameters including the core thickness, honeycomb wall thickness, and aspect ratio a/b under a certain perimeter are taken as the design variables of the sandwich plate. The core thickness ranges from 2 mm to 9 mm, the honeycomb wall thickness ranges from 0.5 mm to 3 mm, and a/b ranges from 0.208 to 4.8 with a certain circumference of $a + b = 0.58\,\text{m}$. The changes of these design variables will affect the structural stiffness, and thus affect the natural frequency. In order not to reduce the stiffness too much, the change in the fundamental frequency is added to the objective function. The objective function is expressed as

$$\max f(x) = (1-\eta)L_{\text{STL},1\,000}(x) + \eta(f_1 - f_0), \tag{22}$$

where η is the weight coefficient, and f_1 and f_0 are the fundamental frequencies after and before the optimization, respectively.

If $\eta = 0.2$, the population number is 20, the number of optimization generations is 40, and the chromosome length is 10. The change trend of the optimal individual and the optimized STL curve at 1 000 Hz are shown in Fig. 13. The optimized parameters are $h_c = 6.997\,3\,\text{mm}$, $a = 0.100\,0\,\text{m}$, $b = 0.48\,\text{mm}$, and $t_h = 0.637\,3\,\text{mm}$. The objective function value at 1 000 Hz after optimization converges to 489.56, and $\Delta L_{\text{STL}} = 21.56\,\text{dB}$. As the incremental of the fundamental frequency exists in the objective function, from the previous studies, we know that as the core thickness decreases and the honeycomb wall thickness increases, the stiffness of the sandwich plate will decrease and the fundamental frequency will decrease. Because the fundamental frequency has a large variation range while the STL value has a small variation range, the change of the fundamental frequency plays a major role when $\eta = 0.2$. Additionally, when a/b is small, the stiffness of the sandwich plate greatly increases and the STL at 1 000 Hz will show a larger value. Therefore, under this condition, the aspect ratio is the dominant factor in the optimized results, and the frequency part in the objective function has a greater

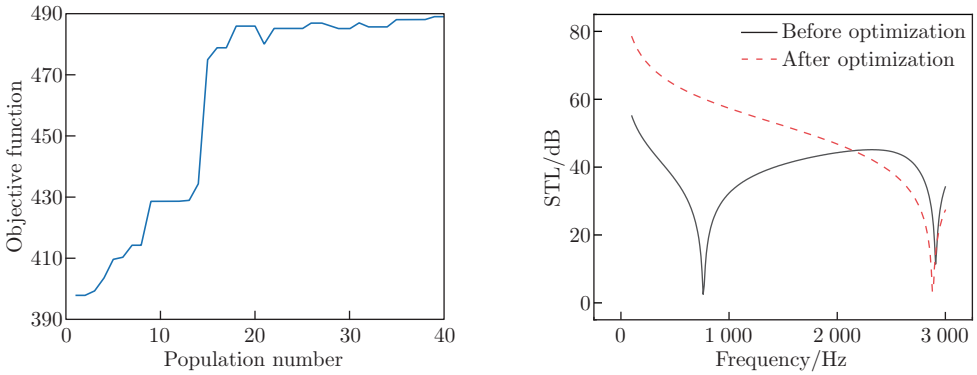

(a) Optimal individual change trend (b) Optimized STL comparison

Fig. 13 Multi-parameter comprehensive optimized results as $\eta = 0.2$ (color online)

effect. In the final optimized result, when the aspect ratio is near the minimum value, the core thickness decreases slightly, the honeycomb wall thickness decreases, and the fundamental frequency increases. When the objective function reaches the maximum, it can be found that the fundamental frequency increases greatly, and the STL value at 1 000 Hz also increases greatly.

In the above example, the weight coefficient is relatively large. In order to more clearly explain the different effects of the weight coefficient on the optimized parameters, we set a smaller value for the weight coefficient, such as $\eta = 0.01$. In this case, the population number is 20, the number of optimization generations is 40, and the chromosome length is 10, the change trend of the optimal individual and the optimized STL curve at 2 000 Hz are depicted in Fig. 14. The optimized parameters are

$$h_c = 5.980\,4\,\text{mm}, \quad a = 0.100\,0\,\text{m}, \quad b = 0.480\,0\,\text{m}, \quad t_h = 0.5\,\text{mm}.$$

The objective function value at 2 000 Hz after optimization converges to 69.96, and the STL at 2 000 Hz after optimization is increased by 5.74 dB. We find that when the weight of the fundamental frequency is lower, the two design variables including the core thickness and the honeycomb wall thickness change to some extent, and the final converged result of the objective function is close to that of STL. Compared with the initial parameters, the two parameters change towards the trend of increasing STL and decreasing stiffness, and the aspect ratio still takes the extreme value. According to the above analysis, the extreme value of the aspect ratio will produce the best optimization effect on the fundamental frequency and STL. Under this condition, the aspect ratio is near the maximum value, which still has an important effect on the optimized result. Simultaneously, the core thickness decreases and the honeycomb wall thickness decreases. When the objective function reaches the maximum, it can be found that the fundamental frequency increases greatly while the STL value at 2 000 Hz increases slightly.

5 Conclusions

Based on the TSDT, a dynamic equation of the sandwich plates with the corrugation and auxetic honeycomb hybrid core is established, and the sound insulation expression is given. The obtained STL curve is validated by the COMSOL simulation, and the effects of the structural parameters on the sound insulation performance of the sandwich plate are discussed. When the frequency of the incident sound wave is near the natural frequency of the system, the sandwich plate resonates, which causes most of the sound wave to be transmitted from the lower surface of the plate, and two troughs of the sound insulation appear on the STL curves. When the

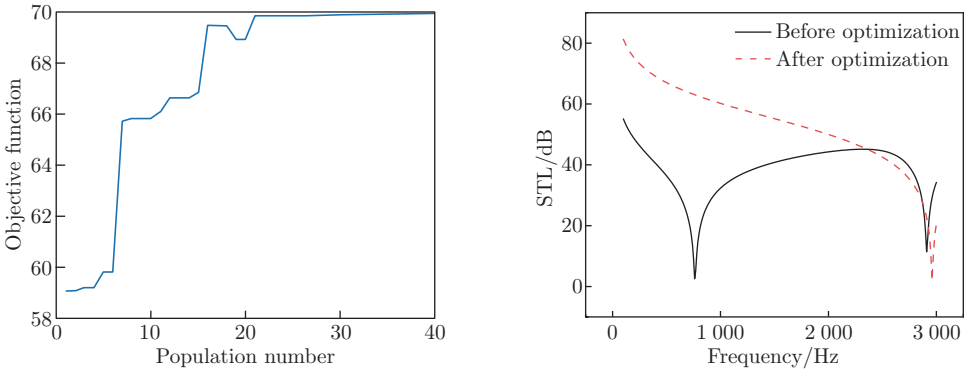

(a) Optimal individual change trend (b) Optimized STL comparison

Fig. 14 Multi-parameter comprehensive optimization results as $\eta = 0.01$ (color online)

natural frequency with geometric parameters changes, the troughs on the STL curves change accordingly.

The genetic algorithm can optimize the STL of the sandwich plate with the corrugation and auxetic honeycomb hybrid core. A stable optimal result can be obtained by giving the appropriate population number, optimization generation number, and chromosome length. Sufficient population can ensure the search range and efficiency, appropriate generations determine the number of iterations and, ensure the convergence of results, and appropriate chromosome length guarantees the precision of optimization variables. According to the actual applications, different optimization variables can be set to optimize the sound insulation of the sandwich plate.

Furthermore, in multi-objective optimization, the weights of different objectives have a great effect on the optimized STL results, and different optimization variables will also have different effects on the objective function. Therefore, it is necessary to take the appropriate weight coefficient to find the optimal solution.

Conflict of interest The authors declare no conflict of interests.

References

[1] TEWARI, K., PANDIT, M. K., BUDARAPU, P. R., and NATARAJAN, S. Analysis of sandwich structures with corrugated and spiderweb-inspired cores for aerospace applications. *Thin-Walled Structures*, **180**, 109812 (2022)

[2] RUI, G., ZHANG, Q., ZHAO, Z., FENG J., and LIU, R. Progress in manufacturing lightweight corrugated sandwich structures and their multifunctional applications. *Mechanics in Engineering*, **39**, 226–239 (2017)

[3] HOHE, J. and BECKER, W. Effective stress-strain relations for two-dimensional cellular sandwich cores: homogenization, material models, and properties. *Applied Mechanics Reviews*, **55**, 61–87 (2002)

[4] ZHUANG, W. Z., YANG, C., and WU, Z. G. Modal and aeroelastic analysis of trapezoidal corrugated-core sandwich panels in supersonic flow. *International Journal of Mechanical Sciences*, **157**, 267–281 (2019)

[5] HOU, W. B., SHEN, Y. X., JIANG, K., and WANG, C. S. Study on mechanical properties of carbon fiber honeycomb curved sandwich structure and its application in engine hood. *Composite Structures*, **286**, 115302 (2022)

[6] SHEN, C., XIN, F. X., and LU, T. J. Theoretical model for sound transmission through finite sandwich structures with corrugated core. *International Journal of Non-Linear Mechanics*, **47**, 1066–1072 (2012)

[7] HAN, B., QIN, K., YU, B., WANG, B., and ZHANG, Q. C. Honeycomb-corrugation hybrid as a novel sandwich core for significantly enhanced compressive performance. *Materials & Design*, **93**, 271–282 (2016)

[8] HAN, B., ZHANG, Z. J., ZHANG, Q. C., ZHANG, Q., LU, T. J., and LU, B. H. Recent advances in hybrid lattice-cored sandwiches for enhanced multifunctional performance. *Extreme Mechanics Letters*, **10**, 58–69 (2016)

[9] ZHANG, Z. J., HAN, B., ZHANG, Q. C., and JIN, F. Free vibration analysis of sandwich beams with honeycomb-corrugation hybrid cores. *Composite Structures*, **171**, 335–344 (2017)

[10] ZHANG, Z. J., ZHANG, Q. C., ZHANG, D. Z., LI, Y, JIN, F., and FANG, D. N. Enhanced mechanical performance of brazed sandwich panels with high density square honeycomb-corrugation hybrid cores. *Thin-Walled Structures*, **151**, 106757 (2020)

[11] LIU, J. Y. and LIU, H. T. Energy absorption characteristics and stability of novel bionic negative Poisso's ratio honeycomb under oblique compression. *Engineering Structures*, **267**, 114682 (2022)

[12] LI, Z., WANG, B. L., WANG, K. F., and ZHENG, L. Improving thermomechanical properties of cracked brittle honeycombs by negative Poisson's ratio effect. *Composite Structures*, **266**, 113825 (2021)

[13] SHAO, Y. J., MENG, J. X., MA, G. H., REN, S., FANG, L., CAO, X. F., LIU, L. W., LI, H. M., WU, W. W., and XIAO, D. B. Insight into the negative Poisson's ratio effect of the gradient auxetic reentrant honeycombs. *Composite Structures*, **274**, 114366 (2021)

[14] XIAO, P., ZHONG, Y. F., JIE, S., and ZHENG, S. Global buckling analysis of composite honeycomb sandwich plate with negative Poisson's ratio using variational asymptotic equivalent model. *Composite Structures*, **264**, 113721 (2021)

[15] XU, F., YU, K., and HUA, L. In-plane dynamic response and multi-objective optimization of negative Poisson's ratio (NPR) honeycomb structures with sinusoidal curve. *Composite Structures*, **269**, 114018 (2021)

[16] LI, F. L., YUAN, W. H., and ZHANG, C. Z. Free vibration and sound insulation of functionally graded honeycomb sandwich plates. *Journal of Sandwich Structures and Materials*, **24**, 565–600 (2022)

[17] XIN, F. X. and LU, T. J. Sound radiation of orthogonally rib-stiffened sandwich structures with cavity absorption. *Composite Science and Technology*, **70**, 2198–2206 (2010)

[18] LIN, C. G., WEN, G. L., YIN, H. F., WANG, Z. P., LIU, J., and XIE, Y. M. Revealing the sound insulation capacities of TPMS sandwich panels. *Journal of Sound and Vibration*, **540**, 117303 (2022)

[19] GRIESE, D., SUMMERS, J. D., and THOMPSON, L. The effect of honeycomb core geometry on the sound transmission performance of sandwich panels. *Journal of Vibration and Acoustics*: *Transactions of the ASME*, **137**, 021011 (2015)

[20] MENG, H., GALLAND, M. A., ICHCHOU, M., XIN, F. X., and LU, T. J. On the low frequency acoustic properties of novel multifunctional honeycomb sandwich panels with micro-perforated faceplates. *Applied Acoustics*, **152**, 31–40 (2019)

[21] OLIAZADEH, P., FARSHIDIANFAR, A., and CROCKER, M. J. Experimental study and analytical modeling of sound transmission through honeycomb sandwich panels using SEA method. *Composite Structures*, **280**, 114927 (2022)

[22] XUE, Y., LI, J. Q., WANG, Y., SONG, Z. G., and KRUSHYNSKA, A. O. Widely tunable magnetorheological metamaterials with nonlinear amplification mechanism. *International Journal of Mechanics Science*, **264**, 108830 (2024)

[23] LI, J. Q., XUE, Y., and LI, F. M. Active band gap control of magnetorheological meta-plate using frequency feedback control law. *Journal of Sound and Vibration*, **567**, 118076 (2023)

[24] DONG, H. W., SHEN, C., ZHAO, S. D., QIU, W. B., ZHENG, H. R., ZHANG, C. Z., CUMMER, S. A., WANG, Y. S., FANG, D. A., and CHENG, L. Achromatic metasurfaces by dispersion customization for ultra-broadband acoustic beam engineering. *National Science Review*, **12**, 185–195 (2022)

[25] YUAN, W. H., LIAO, H. T., GAO, R. X., and LI, F. L. Vibration and sound transmission loss characteristics of porous foam functionally graded sandwich panels in thermal environment. *Applied Mathematics and Mechanics* (*English Edition*), **44**(6), 897–916 (2023) https://doi.org/10.1007/s10483-023-3004-7

[26] FU, T., CHEN, Z. B., YU, H. Y., LI, C. G., and ZHAO, Y. Z. Thermal buckling and sound radiation behavior of truss core sandwich panel resting on elastic foundation. *International Journal of Mechanical Sciences*, **161**, 105055 (2019)

[27] SONG, Y. B., WEN, J. H., TIAN, H., LU, X. G., LI, Z. C., and FENG, L. P. Vibration and sound properties of metamaterial sandwich panels with periodically attached resonators: simulation and experiment study. *Journal of Sound and Vibration*, **489**, 115644 (2020)

[28] THAMBURAJ, P. and SUN, J. Q. Optimization of anisotropic sandwich beams for higher sound transmission loss. *Journal of Sound and Vibration*, **254**, 23–36 (2002)

[29] TSAI, Y. T., PAWAR, S. J., and HUANG, J. H. Optimizing material properties of composite plates for sound transmission problem. *Journal of Sound and Vibration*, **335**, 174–186 (2015)

[30] KIM, H., GOO, S., JUNG, J., and WANG, S. Design optimization of a cellular-type noise insulation panel to improve transmission loss at low frequency. *Journal of Sound and Vibration*, **447**, 105–119 (2019)

[31] JIE, Z., ATUL, B., and XIN, Z. Optimization for sound transmission through a double-wall panel. *Applied Acoustics*, **74**, 1422–1428 (2013)

[32] DENLI, H. and SUN, J. Q. Structural-acoustic optimization of sandwich structures with cellular cores for minimum sound radiation. *Journal of Sound and Vibration*, **301**, 93–105 (2006)

[33] ZHANG, G. H., ZHENG, H., and ZHU, X. S. Optimization of composite plates with viscoelastic damping layer for high sound transmission loss under stiffness and strength constraints. *Composite Structures*, **306**, 116563 (2023)

[34] JIANG, F., YANG, S., QI, C., LIU, H. T., REMENNIKOV, A., and PEI, L. Z. Blast response and multi-objective optimization of graded re-entrant circular auxetic cored sandwich panels. *Composite Structures*, **305**, 116494 (2023)

[35] DONG, H. W., ZHAO, S. D., WANG, Y. S., and ZHANG, C. Z. Topology optimization of anisotropic broadband double-negative elastic metamaterials. *Journal of the Mechanics and Physics of Solids*, **105**, 54–80 (2017)

[36] DONG, H. W., ZHAO, S. D., XIANG, P., WANG, B., ZHANG, C. Z., CHENG, L., WANG, Y. S., and FANG, D. A. Porous-solid metaconverters for broadband underwater sound absorption and insulation. *Physical Review Applied*, **19**, 044074 (2023)

[37] WANG, D., XIE, S. C., YANG, S. C., and LI, Z. Sound absorption performance of acoustic metamaterials composed of double-layer honeycomb structure. *Journal of Central South University*, **28**, 2947–2960 (2021)

[38] HU, J., YAO, S., and HUANG, X. D. Topological design of sandwich structures filling with poroelastic materials for sound insulation. *Finite Elements in Analysis & Design*, **199**, 103650 (2022)

[39] REDDY, J. N. *Mechanics of Laminated Composite Plates and Shells*: *Theory and Analysis*, CRC Press, New York (2004)